

Three-Dimensional Dynamics of Breakout Afterburner Ion Acceleration Using High-Contrast Short-Pulse Laser and Nanoscale Targets

L. Yin,^{1,*} B. J. Albright,¹ K. J. Bowers,¹ D. Jung,² J. C. Fernández,¹ and B. M. Hegelich^{1,2}

¹*Los Alamos National Laboratory, Los Alamos, New Mexico 87545, USA*

²*Department für Physik, Ludwig-Maximilians-Universität München, Garching, Germany*

(Received 20 March 2010; published 20 July 2011)

Breakout afterburner (BOA) laser-ion acceleration has been demonstrated for the first time in the laboratory. In the BOA, an initially solid-density target undergoes relativistically induced transparency, initiating a period of enhanced ion acceleration. First-ever kinetic simulations of the BOA in three dimensions show that the ion beam forms lobes in the direction orthogonal to laser polarization and propagation. Analytic theory presented for the electron dynamics in the laser ponderomotive field explains how azimuthal symmetry breaks even for a symmetric laser intensity profile; these results are consistent with recent experiments at the Trident laser facility.

DOI: 10.1103/PhysRevLett.107.045003

PACS numbers: 52.38.Kd, 52.50.Jm, 52.59.-f

Laser-ion accelerators use intense ($I > 10^{18}$ W/cm²), short-pulse lasers and thin, solid-density targets to produce electric fields, of order 10 TV/m, orders of magnitude higher than in conventional accelerators. The high-current (>kA) and low transverse emittance ($< 10^{-3} \pi$ mm mrad [1]) of these beams are promising for applications such as ion-driven fast-ignition inertial fusion [2] and hadron therapy [3]. To date, most experiments [4] examined μ m-scale and thicker targets, where target normal sheath acceleration [5] dominates. More recently, simulations and experiments [6–9] showed improved efficiency and ion energy with thinner targets. Typically, the finite prepulse and pedestal of a high intensity, short-pulse laser destroy sub- μ m-scale targets before arrival of the main pulse; however, high laser contrast [10] allows the use of sub- μ m- to nm-scale targets, enabling new acceleration mechanisms, such as the breakout afterburner (BOA) [8,9] [linear polarization (LP)] and radiation pressure acceleration [11] [circular polarization (CP)].

In this work, the BOA is modeled using the three-dimensional (3D), relativistic, electromagnetic, charge-conserving, particle-in-cell (PIC) code VPIC [12]. Ion acceleration is examined at a peak laser intensity $I_0 = 10^{21}$ W/cm². In the simulations, a LP laser with $\lambda_0 = 1$ μ m enters the domain from the left boundary and interacts with a target 5 μ m from the boundary. The laser pulse has a temporal intensity profile $I(t) = I_0 \sin^2(t\pi/\tau)$, where $\tau = 2 \times \text{FWHM}$, and its transverse spatial profile is Gaussian with best focus on the target. The target is 30 nm thick ($\sim 5c/\omega_{pe}$, where c/ω_{pe} is the skin depth and ω_{pe} the initial electron plasma frequency) and comprises electrons and C^{6+} ions at density $n_e/n_{cr} = 660$ (i.e., near solid density; n_e is the electron density and n_{cr} is the critical density) with a step-function density profile at $t = 0$. An initial electron temperature T_e of 165 keV is used to resolve the initial Debye length ($T_i = 10$ eV initially). Absorbing boundary conditions are used for particles and fields.

In the left-hand frames in Fig. 1, we show results from a 2D simulation with spatial domain 50×50 μ m in the (x, z) plane (the target width is 50 μ m); x is the laser propagation direction and z is the transverse direction. The pulse has duration $\tau = 156$ fs polarized along y with a Gaussian profile $E_y \sim \exp(-z^2/w^2)$, where $w = 4$ μ m. The simulation cell size is $0.4\lambda_D^0$ (which is 1.4 nm) in x and z , with $\lambda_D^0 = (T_e/4\pi n_e e^2)^{1/2}$ representing initial electron Debye length.

Since the target is highly overdense, laser propagation into the target is limited initially to a skin depth layer at the front surface. Hot electrons produced at the front surface propagate to the back of the target where the laser field is absent; return current electrons migrate to the left of the target, where they are heated by the laser. In the BOA, the nm-scale target expands longitudinally as finite electron temperature, which entails finite electron pressure, increases rapidly as the laser heats the electrons. As the target expands, the peak density decreases and the skin depth increases by virtue of the lower local electron density and higher Lorentz factor $\gamma = \sqrt{1 + p_e^2/(m_e c)^2}$, where p_e is electron momentum. Consequently, the laser penetration depth increases, leading to volumetric heating of all the electrons in the target within the laser spot. We define the time t_1 as when $n_e \approx \gamma n_{cr}$ and the target becomes relativistically transparent; t_1 marks the start of the BOA stage and the main ion acceleration.

Before transparency, the accelerating electric field E_x is determined by the distribution of hot electrons produced at the front layer of the target. The maximum ion energy during this early phase is small, less than 100 MeV. After transparency, enhanced E_x results from electron dynamics in the laser field. A relativistic Buneman instability [9], which efficiently couples electron momentum to ion momentum, appears to be operative during this phase. In Fig. 1, we show on-axis carbon ion phase space from a 1- μ m average in z centered on the

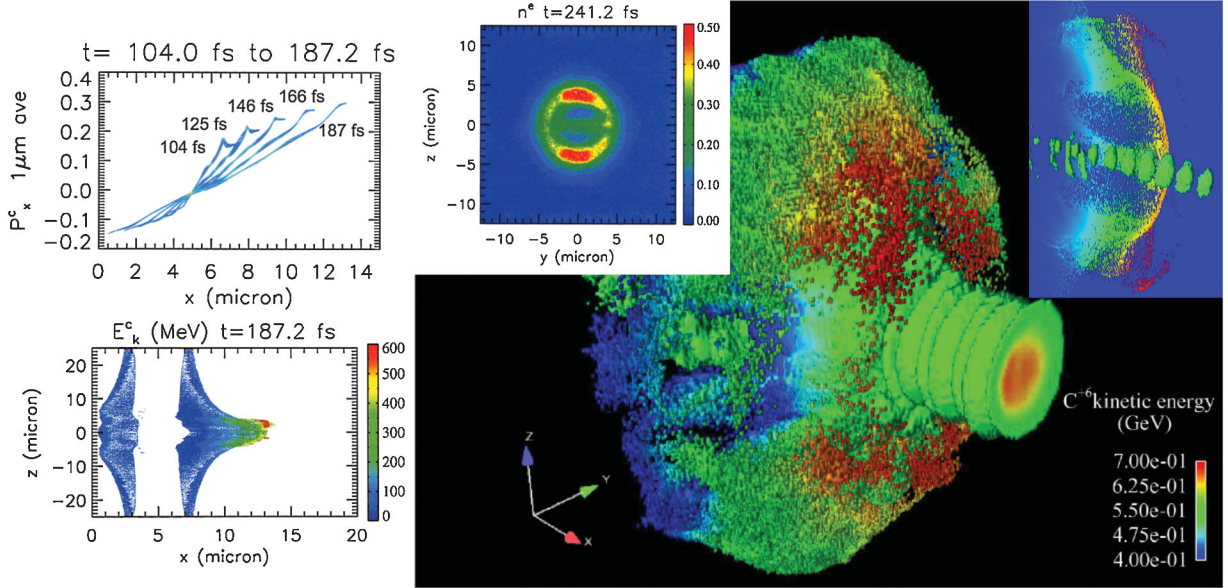


FIG. 1 (color). Left-hand panels: C^{6+} ion momentum ($p_i/m_i c$) phase space distribution on axis (top; obtained along a $1\text{-}\mu\text{m}$ average over z centered on the laser axis at $z = 0$) and kinetic energy spatial distribution (bottom) during relativistic transparency from a 2D BOA simulation. Right: 3D simulation of BOA showing lobes of electron density and high energy ions in the direction z orthogonal to the laser polarization (y). Shown at time $t \approx t_2$ are isosurfaces of C^{6+} energy between 400–700 MeV and the laser at the center; in the left-hand inset are lobes of n_e (obtained from averaging between $x = 10\text{--}20 \mu\text{m}$); in the right-hand inset, contours of C^{6+} energy distribution in (x, z) are displayed in a cut plane through the laser axis, overlaid with an E_x isosurface.

laser axis at $z = 0$ (top left frame) during the main acceleration phase from time $t = 104$ fs (shortly after t_1) to $t_2 = 187$ fs, the time when the peak target density $n_e \approx n_{cr}$. At this time, most of the laser pulse has propagated through the target plasma. The carbon ions comove with the peak in E_x . This results in a peak in the ion momentum, displayed in a time sequence in the top left frame, which corresponds to a monoenergetic carbon beam in the kinetic energy spectrum. For example, at $t = 104$ fs, the on-axis carbon ion energy spectrum has a monoenergetic feature centered around 150 MeV. The spatial distribution of carbon kinetic energy E_k^c at the end of the acceleration at $t = 187$ fs (t_2) is shown in the bottom left frame, where the highest energy ions are found off axis. The on-axis charge density profiles for e^- and C^{6+} indicate that the electrons are depleted from the center of the laser pulse. (This behavior is the 2D analogue of the electron density lobes discussed below and shown in Fig. 2.) This results in transverse acceleration and the presence of off-axis, high energy ions with maximum energy ~ 600 MeV.

Shown in the right-hand panels in Fig. 1 is a 3D simulation of the BOA carried out in a spatial volume $20 \times 25 \times 25 \mu\text{m}$ with $n_e/n_{cr} = 660$ initially. The laser pulse has duration $\tau = 312$ fs and is polarized along y with a Gaussian profile $E_y \sim \exp[-(y^2 + z^2)/w^2]$, where $w = 4 \mu\text{m}$. The simulation cell size is $1.7\lambda_D^0$ (5.95 nm) in x and $3.4\lambda_D^0$ (11.9 nm) in y and z ; 14×10^9 cells and 21×10^9 particles are used (500 particles per cell for each species) [13]. The 3D simulation results support our 2D findings, but with differences: as before, the BOA begins when the target becomes relativistically transparent, at

time $t_1 = 96$ fs when the on-axis kinetic energy spectrum of carbon ions have a monoenergetic peak with maximum energy ~ 90 MeV; the BOA ends at $t_2 = 241$ fs, when peak density $n_e \sim n_{cr}$. At t_2 , the carbon ions have a monoenergetic peak 600–700 MeV off axis, whereas the maximum energy on axis is 560 MeV. Data around t_2 are shown in the right-hand panels in Fig. 1, where isosurfaces for E_k^c between 400–700 MeV are displayed with isosurfaces of E_y^2 for the laser at the center region. Contours of carbon kinetic energy distribution in (x, z) are shown in the right-hand inset in a cut plane through the laser axis at $y = 0$, overlaid with an isosurface of E_x which peaks at the 3rd node from the right, where peak carbon density is located. The peak carbon density comoves with the peak accelerating field and the highest energy ions are found off-axis along the direction perpendicular to the laser polarization in a pair of ion beam lobes. (Ion acceleration dynamics during relativistic transparency from the 3D simulation are shown in the simulation movie [14] accompanying Fig. 1.)

It is difficult to derive analytically the full 3D dynamics of the BOA; however, insight can be gained from the ponderomotive (PM) dynamics in the laser field in the 2D plane perpendicular to laser propagation. Let us consider the response of a relativistic electron fluid to a LP laser beam of finite transverse extent in the large- a_0 limit [15]. The transverse continuity and momentum Eulerian fluid equations (neglecting pressure in the transverse dynamics) are $\frac{\partial n_e}{\partial t} + \nabla \cdot (n_e \mathbf{v}_e) = 0$ and $(\frac{\partial}{\partial t} + \mathbf{v}_e \cdot \nabla) \mathbf{p}_e = -e(\mathbf{E} + \frac{\mathbf{v}_e}{c} \times \mathbf{B})$. The fields n_e , \mathbf{p}_e , and \mathbf{v}_e are defined as $n_e = \langle 1 \rangle_p$, $\mathbf{p}_e = \langle \mathbf{p} \rangle_p / n_e$, $\mathbf{v}_e = \langle \mathbf{p} / m_e \gamma \rangle_p / n_e$, where

$\langle h \rangle_p \equiv \int d^3p h f_e(x, \mathbf{p}, t)$ is a lab-frame momentum-space average over electron distribution function f_e . In the radiation gauge, ϕ is the instantaneous Coulomb potential. The laser field behind the target is evanescent and small prior to t_1 and the plasma is initially at rest, so vorticity can be omitted and the momentum equation becomes

$$\frac{\partial}{\partial t} \left(\mathbf{p}_e - \frac{e\mathbf{A}}{c} \right) \approx -m_e c^2 \nabla \gamma - \nabla \phi. \quad (1)$$

We let $A(x, t) = \hat{y}A(x, t) \cos(kx - \omega t)$, with envelope A varying slowly in time after a rapid turn-on, and assume a pulse localized in space with azimuthal symmetry. For economy of notation, define $s \equiv ct/\lambda_0$, $\boldsymbol{\rho} \equiv \mathbf{r}/\lambda_0$, and normalize \mathbf{p}_e to $m_e c$ and A and ϕ to $m_e c^2/e$.

Perpendicular electron momentum in (1) can be written as a sum of oscillatory and ‘‘secular’’ (nonoscillatory) components $\mathbf{p}_{e\perp} = \mathbf{p}_{e\perp}^f + \mathbf{p}_{e\perp}^s$. To leading order in the limit of relativistic laser intensity and small transverse variation of the envelope, $\mathbf{p}_{e\perp}^f \approx A$. (‘‘Parallel’’ and ‘‘perpendicular’’ are relative to x , the direction of laser propagation.) The secular component of momentum obeys

$$\frac{\partial \mathbf{p}_{e\perp}^s}{\partial s} = -\nabla'_\perp \left\langle \sqrt{1 + p_{e\parallel}^2 + A^2 + 2\mathbf{p}_{e\perp}^s \cdot \mathbf{A} + p_{e\perp}^{s2}} + \phi \right\rangle, \quad (2)$$

where $\langle \rangle$ indicate a time average over a laser period and $\nabla'_\perp \equiv \lambda_0 \nabla_\perp$.

Since $A(r)$ is axisymmetric, $\mathbf{p}_{e\perp}^s$ points (dominantly) radially outward from the center of the laser pulse as the familiar ponderomotive expulsion of plasma from regions of strong laser field. To produce the observed lobes, an $m = 2$ (i.e., $\cos 2\theta$ or $\sin 2\theta$, where θ is the angle between \hat{y} and $\mathbf{p}_{e\perp}$) dependence must arise in the plasma response to the laser field. The dot product in (2) indeed yields an $m = 2$ variation, though as a small perturbation. Let us order asymptotically in $\epsilon \sim |\mathbf{p}_{e\perp}^s|/A_0$ and define

$\gamma_0 \equiv \sqrt{1 + p_{e\parallel}^2 + A^2}$, $\bar{\gamma}_0 \equiv \langle \gamma_0 \rangle$, $\bar{f} \equiv \langle \gamma_0^{-1} \rangle$, $\bar{g} \equiv \langle A^2 \gamma_0^{-3} \rangle / 2$. Equation (2) can be expanded to $\mathcal{O}(\epsilon^4)$ as

$$\frac{\partial \mathbf{p}_{e\perp}^s}{\partial s} \approx -\nabla'_\perp \left[\bar{\gamma}_0 + \frac{\epsilon^2 p_{e\perp}^{s2}}{2} (f - g - g \cos 2\theta) + \phi \right], \quad (3)$$

which has an $\mathcal{O}(\epsilon^2)$ $m = 2$ variation. A larger, $\mathcal{O}(\epsilon)$ $m = 2$ asymmetry is found in the continuity equation

$$\begin{aligned} \frac{\partial n_e^s}{\partial s} &= -\nabla' \cdot \left\langle \frac{n_e \mathbf{p}_e}{\gamma} \right\rangle \\ &\approx -\nabla' \cdot (\epsilon n_s p_{e\perp}^s) [\hat{r}(f - g - g \cos 2\theta) + \hat{\theta} g \sin 2\theta]. \end{aligned} \quad (4)$$

As $\mathbf{p}_{e\perp}^s$ grows to finite value, $\mathbf{p}_{e\perp}^s \cdot \mathbf{p}_{e\perp}^f$ in γ^{-1} becomes finite and leads, in the time average, to smaller γ^{-1} and thus smaller $\langle \mathbf{v}_{e\perp} \rangle$. (Applying this analysis to a CP beam yields neither $m = 2$ asymmetry nor lobes; nor are lobes found in 3D VPIC simulations of relativistic transparency with CP light).

To verify these dynamics, we evolve the 2D, two-fluid (e^- and C^{+6}) hydrodynamics where the e^- fluid obeys (2) and (4). A Lax solver [16] evolves the e^- and ion fluid equations, which are solved on a 150×150 mesh. Results are shown in Figs. 2(e) and 2(f) for a LP laser with intensity 10^{22} W/cm² and spot radius 1 μm , values similar to those obtained in the 3D VPIC simulation near the back of the expanding target where the lobes form. Only plasma beneath the peak of the laser pulse (and not the wings of the pulse) is transparent at t_1 and relativistic laser self-focusing occurs in this channel. Thus, the laser intensity profile in the 2D hydrosimulation has smaller diameter, but higher intensity than the initial laser pulse. (Ion and electron charge densities are uniform initially, $n_e^0 = Z_i n_i^0 = 10 n_{cr}$.)

The collective dynamics of electrons in a LP laser field admit $m = 2$ variation in e^- density and, consequently, the possibility of ion lobe formation. A necessary condition is

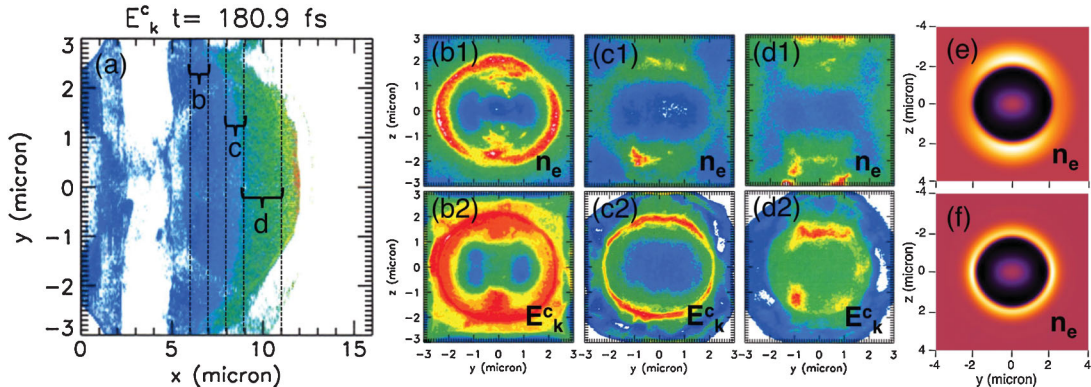


FIG. 2 (color). Ion lobes form near the front of the ion beam. Shown in (a)–(d) are 3D VPIC simulation results of the BOA at time $t = 180.9$ fs during transparency. Panel (a) is $E_k^c(x, y, z = 0)$ and depicts regions over which the data are averaged in panels (b) ($x = 6\text{--}7 \mu\text{m}$), (c) ($8\text{--}9 \mu\text{m}$), and (d) ($9\text{--}11 \mu\text{m}$); in (b)–(d), averages of n_e and E_k^c are displayed. (e), (f) n_e from 2D hydromodeling without and with ES forces from the ions on the expelled electrons, respectively (shown after 3 fs). See text for explanation. [The 3D simulation is carried out at high resolution with cell size $dx = 0.21\lambda_D^0$ ($0.12c/\omega_{pe}^0$) and $dy = dz = 3.46\lambda_D^0$ ($\sim 2c/\omega_{pe}^0$) at peak intensity $I_0 = 5 \times 10^{21}$ W/cm² with an $f/1$ laser.]

that $p_{e\perp}^s$ becomes finite and at least a modest fraction of $\tilde{\gamma}_0$ (so ϵ is not truly infinitesimal) before electrostatic (ES) forces from the ion background overcome the electron PM motion. This can be accomplished for a short time in 2D for a tightly focused beam: neglecting the ES force in (2) and balancing remaining terms yields the electron lobe formation time $s_{\text{lobe}} \sim \tilde{\gamma}_0^{\text{max}}$. From Ampère's law and assuming relativistic radial flow ($v_{\perp} \approx c$), we get the ES force $\nabla'_{\perp} \langle \phi \rangle \sim s \lambda^2 / \rho_e^2$, where ρ_e is the collisionless skin depth. In order for the ES force to not dominate before s_{lobe} , $\tilde{\gamma}_0^{\text{max}} > (r_{\text{spot}} / \rho_e)^2$. The larger the laser beam diameter, the gentler the PM force gradients and the larger the relative strength of the ES force, so the less pronounced the lobes. However, even for small-diameter beams, in 2D geometry, the ES force from the ion background will arrest the electron outflow eventually, leading to azimuthally symmetric ion and electron beams [see Fig. 2(f)]. Indeed, we find this in our 3D VPIC simulation, as shown in Figs. 2(b1) and 2(b2), which are n_e and E_k^c , respectively, averaged over $6 < x < 7 \mu\text{m}$. Near the rightmost edge of the expanding ion layer, the dynamics change: The electrons drift in the direction of the laser and make a pair of jets in the (x, z) plane about the laser axes at the edge of the expanding ion layer [compare Fig. 2, panels 2(b1), 2(c1), and 2(d1)]. Near this edge, geometric divergence effects diminish the electrostatic forces and the ES field is no longer 2D-like. Consequently, the electron PM dynamics in the plane perpendicular to the laser propagation resemble more those of electrons in the absence of an ion background [Fig. 2(e)]. In the 3D VPIC simulation, as one moves toward the front the ion beam, such a transition from 2D-like electron-ion to 3D-like electron-only dynamics is observed. In Figs. 2(c1) and 2(c2) (averaged over $x = 8\text{--}9 \mu\text{m}$), n_e is bunched along z , yet the ions remain azimuthally symmetric, having not yet had time to move appreciably in z . In Figs. 2(d1) and 2(d2) (averaged over $x = 9\text{--}11 \mu\text{m}$), the lobes in n_e have diverged farther and a large, z -aligned ES field forms, which accelerates the front of the ion beam into lobes.

In summary, kinetic simulations of the BOA show dramatic acceleration of ions when the target becomes relativistically transparent to the laser. For tightly focused beams, the high energy ions form a pair of lobes in the direction orthogonal to the laser polarization and propagation. These lobes are likely to originate from $m = 2$ bunching in the electron density from ponderomotive, collective motion of electrons in the laser field, an inherently 3D, collective feature that cannot be captured in lower dimensional simulations or single-particle orbit studies. BOA ion acceleration during relativistic transparency has been validated by experiments [17] in the Trident laser facility at Los Alamos National Laboratory, and, as predicted here, the highest energy carbon ions are found in off-axis lobes [18]. As a final note, the theory predicts that the angle of

propagation of the lobes should depend on gradients of the laser ponderomotive force; consequently, a higher laser intensity or tighter focus should increase this angle. Future measurements using a new, wide-angle ion spectrometer [19] will test this hypothesis.

Work performed under the auspices of the U.S. Department of Energy by the LANS, LLC LANL, and supported by LDRD and DOE OFES. We thank P. Weber and J. Margulies for assistance with visualization and acknowledge useful discussions with the Trident short-pulse team and C. Huang and H.-C. Wu. Simulations were run on ASC Roadrunner.

*lyin@lanl.gov

- [1] T. E. Cowan *et al.*, *Phys. Rev. Lett.* **92**, 204801 (2004).
- [2] M. Roth *et al.*, *Phys. Rev. Lett.* **86**, 436 (2001); M. Temporal, J. J. Honrubia, and S. Atzeni, *Phys. Plasmas* **9**, 3098 (2002); J. C. Fernandez *et al.*, *Nucl. Fusion* **49**, 065004 (2009); J. J. Honrubia *et al.*, *Phys. Plasmas* **16**, 102701 (2009).
- [3] G. H. Hartmann *et al.*, *Phys. Med. Biol.* **44**, 1193 (1999).
- [4] A. Maksimchuk *et al.*, *Phys. Rev. Lett.* **84**, 4108 (2000); R. Snavely *et al.*, *Phys. Rev. Lett.* **85**, 2945 (2000); S. Hatchett *et al.*, *Phys. Plasmas* **7**, 2076 (2000); M. Hegelich *et al.*, *Phys. Rev. Lett.* **89**, 085002 (2002); M. Roth *et al.*, *Phys. Rev. ST Accel. Beams* **5**, 061301 (2002); B. M. Hegelich *et al.*, *Nature (London)* **439**, 441 (2006).
- [5] S. C. Wilks *et al.*, *Phys. Plasmas* **8**, 542 (2001).
- [6] Y. Sentoku *et al.*, *Phys. Plasmas* **10**, 2009 (2003).
- [7] J. Fuchs *et al.*, *J. Phys. IV* **133**, 1151 (2006).
- [8] L. Yin *et al.*, *Laser Part. Beams* **24**, 291 (2006).
- [9] L. Yin *et al.*, *Phys. Plasmas* **14**, 056706 (2007); B. J. Albright *et al.*, *Phys. Plasmas* **14**, 094502 (2007).
- [10] Rahul C. Shah *et al.*, *Opt. Lett.* **34**, 2273 (2009).
- [11] A. P. L. Robinson *et al.*, *New J. Phys.* **10**, 013021 (2008); O. Klimo *et al.*, *Phys. Rev. ST Accel. Beams* **11**, 031301 (2008); X. Q. Yan *et al.*, *Phys. Rev. Lett.* **100**, 135003 (2008); A. Macchi, S. Veghini, and F. Pegoraro, *Phys. Rev. Lett.* **103**, 085003 (2009).
- [12] K. J. Bowers *et al.*, *Phys. Plasmas* **15**, 055703 (2008).
- [13] Higher resolution 3D simulations with tighter laser focus ($f/1$) and increased particle numbers shown in Fig. 2 confirm that the formation of lobes is physical and not a numerical artifact. See discussion in L. Yin *et al.*, *Phys. Plasmas* **18**, 063103 (2011).
- [14] See Supplemental Material at <http://link.aps.org/supplemental/10.1103/PhysRevLett.107.045003> for a movie of the 3D ion acceleration dynamics.
- [15] E. A. Startsev and C. J. McKinstrie, *Phys. Rev. E* **55**, 7527 (1997).
- [16] W. H. Press, S. A. Teukolsky, W. T. Vetterling, and Brian P. Flannery, *Numerical Recipes in C* (Cambridge, New York, 1988), 2nd ed., p. 837.
- [17] A. Henig *et al.*, *Phys. Rev. Lett.* **103**, 045002 (2009).
- [18] B. M. Hegelich *et al.*, *Nucl. Fusion* **51**, 083011 (2011).
- [19] D. Jung *et al.*, *Rev. Sci. Instrum.* **82**, 043301 (2011).